Journal Pre-proof

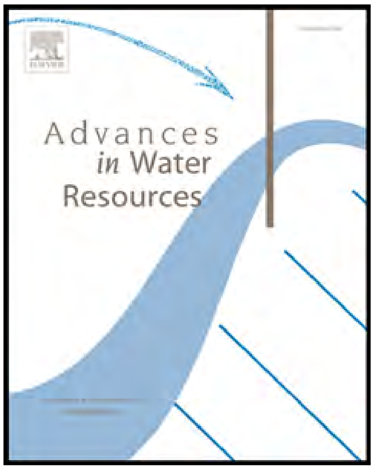

2D experiments and numerical simulation of the oscillatory shallow flow in an open channel lateral cavity

A. Navas-Montilla, S. Martínez-Aranda, A. Lozano, I. García-Palacín, P. García-Navarro

PII: S0309-1708(20)31194-5
DOI: https://doi.org/10.1016/j.advwatres.2020.103836
Reference: ADWR 103836

To appear in: *Advances in Water Resources*

Received date: 11 March 2020
Revised date: 24 November 2020
Accepted date: 16 December 2020

Please cite this article as: A. Navas-Montilla, S. Martínez-Aranda, A. Lozano, I. García-Palacín, P. García-Navarro, 2D experiments and numerical simulation of the oscillatory shallow flow in an open channel lateral cavity, *Advances in Water Resources* (2020), doi: https://doi.org/10.1016/j.advwatres.2020.103836

Highlights

- High resolution 2D space-time data of water surface and velocity oscillation are provided.
- Seiche amplitude maps are presented for different oscillation modes.
- A virtually 1D longitudinal seiche is observed for high Froude numbers (Fr = 0.8).
- The experiments are well reproduced using a 2D third order shallow water model.
- The experimental dataset can serve as a benchmark for other numerical models.

2D experiments and numerical simulation of the oscillatory shallow flow in an open channel lateral cavity

A. Navas-Montilla [1,2,*], S. Martínez-Aranda [2,3], A. Lozano [3], I. García-Palacn [2,3], P. García-Navarro [2,3]

[1] *Centro Universitario de la Defensa, Carretera de Huesca s/n, E-50090 Zaragoza, Spain.*
[2] *Fluid Mechanics, Universidad de Zaragoza, Spain*
[3] *LIFTEC-CSIC, Spain*
[*] *Corresponding author: anavas@unizar.es*

Abstract

Steady shallow flows past an open channel lateral cavity can induce the excitation of an eigenmode of a gravity standing wave inside the cavity, called seiche, which may be coupled with the shedding of vortices at the opening of the cavity. The presence of the seiche is of fundamental interest as it enhances the mass exchange between the main channel and the cavity. Measurements of the time evolution of the water surface are not often found in the literature for this type of flows. In this work, an experimental and numerical study of a shallow flow past a channel lateral cavity is carried out. The main novelty is the use of a pioneering non-intrusive experimental technique to measure the water surface at the channel-cavity region. This optical technique offers high resolution 2D data in time and space of the water surface evolution, allowing to determine the relevant features of the seiche oscillation. Such data are supplemented with Particle Image Velocimetry measurements. Furthermore, the experiments are numerically reproduced using a high-resolution depth-averaged URANS shallow water model, under the assumption that shallow water turbulence is mainly horizontal. The experimental and numerical results are analyzed in the frequency domain. High-resolution two-dimensional amplitude oscillation maps of the seiche phenomenon, as well as velocity fields, are presented. The high quality of the experimental data reported in this work makes this data set a suitable benchmark for numerical simulation models in order to evaluate their performance in the resolution of turbulent resonant shallow flows.

Keywords:
Shallow flows; resonance phenomenon; channel lateral cavity; PIV; transient experimental water surfaces; RGB-D sensor

1. Introduction

Shallow water flows are present in a wide variety of scenarios, such as riverine and coastal areas [1, 2]. They are characterized by a water depth smaller than the horizontal dimensions of the flow and those of the relevant wavelength. Shallow flows are usually fully turbulent, with a characteristic length scale of the 3D turbulent eddies smaller than water depth. Furthermore, large scale horizontal vortical structures with a characteristic length larger than the water depth are usually observed in these flows [3]. Such structures normally appear in presence of geometrical singularities. These singularities may span from cavities or obstacles inside the channel, to strong variations in the bed profile or cross sectional area (e.g. compound channels) [3, 4, 5]. As a result, the turbulence spectrum of shallow flows is divided in two separated regions: the low-wavenumber region where the kinetic energy cascade associated to 2D turbulence (i.e. large horizontal vortices) appears and the high-wavenumber region where the 3D kinetic energy cascade is located [3, 6], as depicted in Figure 1. It must be noted that the presence of such large scale coherent vortices on the horizontal plane plays an important role in the mass and momentum exchange between the different flow regions, and even in other aspects of hydro-morphological and even biological interest (e.g. the conveyance of fine sediments in suspension [7, 8], the transport of pollutants [9], etc.).

Shallow flows are also characterized by the presence of a free surface and a bottom surface. Free surface variations are due to the intrinsic mechanisms governing the flow and may sometimes appear in the form of gravity waves. A particular type of gravity waves are seiches, which are standing resonant waves usually appearing in bounded flows such as channel lateral cavities [10, 11, 12, 13]. The complex hydrodynamic patterns arising in presence of lateral cavities play an important role in the bed morphodynamics and other aspects of biological interest. Some authors [15, 16, 17] analyzed the effect of sediment siltation in groyne fields for the sediment budget of rivers. Juez et al. experimentally measured the trapping efficiency of different macro-roughness (i.e. multiple lateral cavities) geometries and their suitability for river restoration purposes [14].

Shallow flows past a lateral cavity can induce the excitation of an eigenmode of a gravity standing wave (i.e. the seiche) inside the cavity, due to the coupling with the hydrodynamical instability associated to the separated shear layer at the opening of the cavity [12, 18]. In [18], it was observed that such coupling is a global phenomenon that persists for regions close to and well above the bottom surface. This was reported to be associated with the presence of large-scale coherent vortical structures in the unstable shear layer. Near the water surface, the undulation of the shear layer gives rise to the formation of highly coherent vortices, which are advected downstream along the shear line and eventually impinge upon the trailing edge of the cavity (i.e. the impingement corner). Close to the bed, the overall undulating pattern is maintained but the degree of coherence is decreased [18]. It must be pointed out that the presence of the seiche is of fundamental interest as the mass exchange between the main channel and the cavity exhibits a substantial enhancement when present [18].

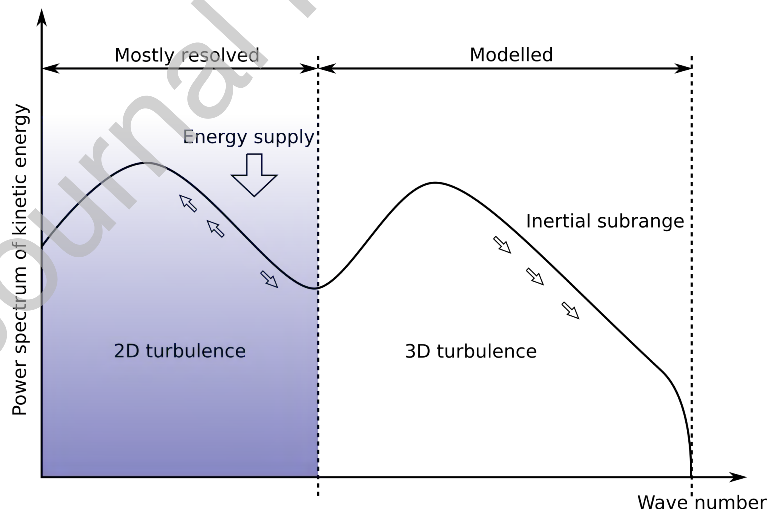

Figure 1: Sketch of the kinetic energy cascade in turbulent shallow water flows and regions of the turbulence spectrum resolved and modelled by the URANS approach. Adapted from [3].

There is an extensive literature dealing with the problem of shallow flows past a lateral cavity. Maybe one of the earliest works is the pioneering study by Kimura and Hosoda [12] where the authors measured and simulated the formation of periodic vortical structures along the opening of the cavity and their coupling with a seiche wave. Later on, Uijttewaal et al. [19], Le Coz et al. [20], Ekmekci and Rockwell [21], Meile et al. [22], Wolfinger et al. [23], Tuna et al. [18], Sanjou and Nezu [24], Uijttewaal [2], Akutina [25] , Mignot et al. [26], Mignot et al. [27] and Perrot-Mignot et al. [28] carried out a series of experimental studies which shed light on the coupling mechanisms and flow structure of these particular configurations. It must be noted that, whereas spatio-temporal velocity measurements are often found in the literature thanks to well-stablished measurement techniques such as Particle Image Velocimetry (PIV), measurements of the time evolution of the water surface are normally carried out at single points. To this end, ultrasonic gauges, pressure gauges and electrically resistive rods are often used. In the last years, special attention has been paid to development of non-intrusive optical techniques able to obtain the spatial-temporal evolution of the flow free surface under controlled conditions [11, 29, 30, 31, 13, 28]. Most of these recent techniques are based on the stereo-refraction principle, consisting of comparing the apparent displacement between a reference pattern and its refracted image. These optical techniques allow the reconstruction of smooth free surface variations with a relatively good accuracy and resolution, but require corrections for optical aberrations, reflections at the free surface and (most of the times) complex experimental setups and processing algorithms.

Numerical studies of shallow flow past a lateral cavity are more scarce. Hinterberger et al. [4] and McCoy et al. [32] presented numerical computations using 2D-depth averaged and 3D LES and RANS models. Recently, Ouro et al. [33] applied a 3D LES model to a channel with symmetrically-distributed lateral bank cavities, throwing light on the exchange processes. Even though the flow patterns show three-dimensional characteristics [33], depth-averaged computations have proved to be successful in the determination of the fundamental features of the flow [12, 34]. The numerical simulation of channels with single and multiple lateral cavities which involve longitudinal and transverse seiches using the shallow water equations (SWE) with turbulence diffusion was addressed in [34]. The model therein used consisted of a 2D depth-averaged (DA) URANS high-resolution model, able to resolve the large-scale coherent vortical structures (see Figure 1) and their inherent coupling with standing gravity waves. The results evidenced that the frequency and amplitude of the seiche can be accurately predicted (and mesh convergence achieved) as long as a high order of accuracy for the approximation of the convective fluxes in combination with a suitable turbulence model is used. Furthermore, it was shown that the model over predicted the magnitude of the velocity in the recirculation region, near the walls [12, 34].

This work aims at the experimental and numerical study of a shallow flow past a lateral cavity with a longitudinal seiche. The aim of the paper is threefold: (a) to study the properties of the seiche and its coupling with the shedding of vortices at the opening of the cavity in a high Froude number channel-cavity configuration; (b) to provide a complete data set which can serve as a benchmark for numerical simulation models to evaluate their performance in the resolution of turbulent resonant shallow flows; (c) to fully assess the performance of the WENO-ADER model in [34] using 2D space-time water surface and velocity measurements. The main novelty of the work is a high resolution spatio-temporal measurement of the water surface elevation, which allows to extract and analyze the relevant features of the seiche, i.e. the spatial distribution of oscillation nodes and anti-nodes and the oscillation modes, supplemented with PIV velocity measurements at channel-cavity region. Furthermore, numerical results for the measured flows are also presented. The numerical simulations are computed by a 2D depth-averaged (DA) URANS high-resolution model. The present set of 2D measured data allows a much more detailed evaluation of the performance of the model using seiche amplitude maps. Only when comparing such data, the actual performance of the model is brought out and we can affirm that we have carried out a proper assessment of the model.

The paper is structured as follows. In Section 2 the experimental setup for the water surface and flow velocity measurement is described. Section Appendix A is devoted to the governing equations and the numerical model. Experimental and numerical 2D high resolution maps of the intensity of the seiche are presented in Section 4. The locations of the oscillation nodes and anti-nodes are clearly evidenced and a good correspondence between experimental and numerical data is also reported. Additionally, the experimental and numerical time-averaged velocity results in the horizontal plane are presented and the spectral analysis of the mean velocity fluctuation in time along different longitudinal cross sections is also presented. The numerical model is used to study the coupling mechanism between the vortex shedding and the seiche. Different phase-portrait representations of the solution in the limit cycle allow to correlate the phases of the shear layer oscillation (i.e. vortex shedding) and the seiche. Finally, the main conclusions are drawn in Section 5. Furthermore, additional information regarding the experimental results has been included: (Appendix B) components of the averaged velocity at the channel-cavity region; (Appendix C) detailed information about processing of the water surface measured data and (Appendix D) the algorithm used for the spectral analysis of the measured water surface evolution.

2. Experimental setup

The experimental facility herein considered consists of a recirculating, free-surface open channel made of methacrylate. The channel is $6\,m$ long with a constant width rectangular cross-section of $B = 24\,cm$. The height of the channel's walls is $H = 16\,cm$. The measurement reach started $2.66\,m$ downstream the channel inlet and was $3.34\,m$ long with 0.25% longitudinal slope. A square lateral cavity $24 \times 24\,cm$ (width to length ratio $W/L = 1$) also made of methacrylate was placed on one side of the channel, separated $1.80\,m$ meters from the measurement reach beginning in order to satisfy the criterion of L/h proposed by Uijttewaal et al. [2] required to guarantee a fully developed flow. The inflow to the channel was from an upstream reservoir, which was fed using a recirculation system from a recovery tank placed at the end of the channel. The inflow discharge was controlled using a flowmeter inserted in the recirculation conduit. The outlet of the channel was set free and far enough to the cavity to avoid the disturbance of the uniform flow at the measurement region. The uniform flow conditions at the measurement reach were varied by adjusting the discharge at the channel inlet. Five different steady experiments with constant inflow discharges Q_{in} were carried out (see Table 1).

Case	Q_{in} (m^3/s)
S1	0.0016
S2	0.0022
S3	0.0028
S4	0.0033
S5	0.0041

Table 1: Inlet discharges for each experiment.

A sketch of the theoretical flow configuration at the channel-cavity region is shown in Figure 2, where the geometry and the main flow structures expected in the channel-cavity region are summarized.

2.1. Water surface measurement

The measurement of the water surface elevation at the channel-cavity region was carried out using a pioneering technique which allows to obtain 2D transient measurements of the flow free surface [35]. A RGB-D sensor (Microsoft Kinect, 2010) was suspended $70\,cm$ above the flume floor, ensuring a good compromise between field-of-view, 2D spatial resolution (millimeters-per-pixel) and depth-accuracy [36], and approximately covering the channel-cavity region. A sketch of the experimental setup is shown in Figure 3. This device provides a sequence of $640 \times 480\,px$ RGB+Depth VGA binary images of the objects placed into its field-of-view. Briefly, the Kinect sensor works using the standard structured light (SL) principle, i.e. projecting an infrared pattern by means of a NIR laser diode at $850\,nm$ wavelength onto the objects. The apparent pattern deformation due to the position and shape of the objects is recorded by a monochrome NIR camera observing from a slightly different angle. This apparent deformation allows the device to produce –in hardware– a depth map for the VGA image. The 2D spatial resolution of the VGA images was $1.4\,mm$ and the depth accuracy was $\sim 1\,mm$ for the distance

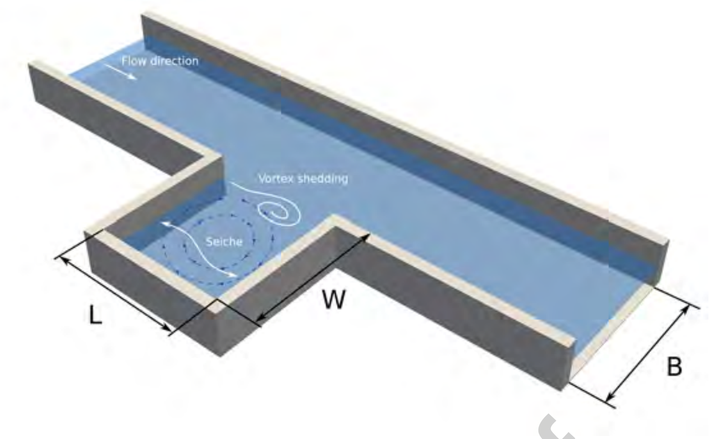

Figure 2: Sketch of the expected flow structures.

between the sensor and the water surface considered in these experiments [37]. In order to allow the sensor to observe the water surface, the projected infrared pattern needs to be reflected by the flow free surface. A simple solution is to tint the water until it is quasi-opaque. In the present work, water was tinted with titanium dioxide (TiO_2) at a concentration of 0.15% in mass. The TiO_2 was previously mixed with the upstream reservoir fluid and the tinted water was recirculated continuously avoiding deposition. The required concentration was calibrated in a separated facility before performing the experiments. This technique allows to directly reflect the infrared points pattern off the water surface, thus not requiring any correction of the measured depth data [35].

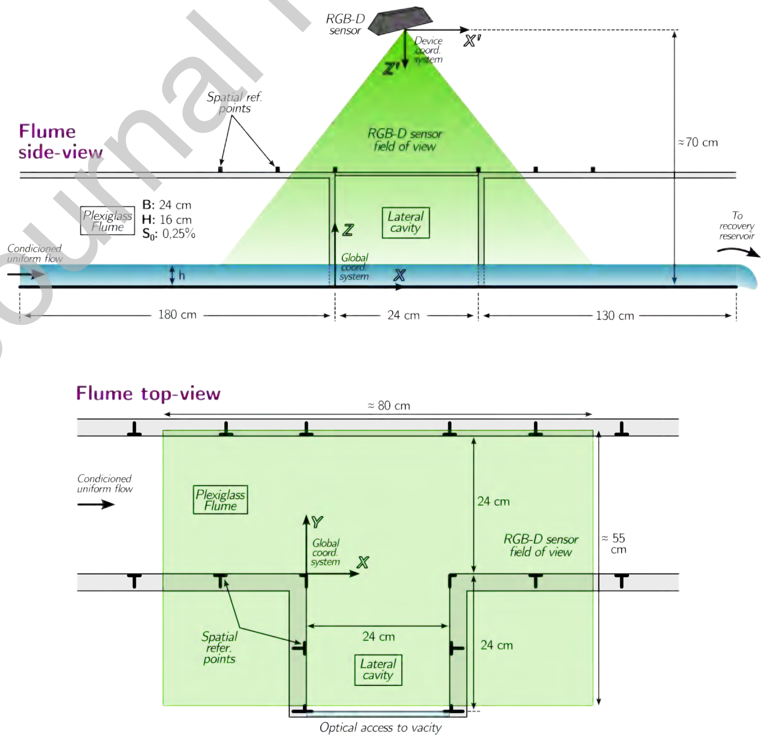

Figure 3: Experimental setup for the water surface elevation measurement using Microsoft Kinect: (top) side-view and (bottom) top-view.

The device streams both the RGB and depth binary images, which are directly recorded in a solid-state disk using an *ad-hoc* C++ code based on the open-source *libfreenect* library [38] with an acquisition rate of $30\,Hz$ approximately. Each captured RGB and depth binary image was timestamped with millisecond resolution. The flow free surface was recorded during $60\,sec$ for each experiment. In order to easily georeference the recorded binary images, spatial reference points were placed on the channel-cavity region within the field-of-view of the RGB-D sensors. The global coordinate system was chosen to agree with the upstream corner of the cavity. Once an experiment was carried out, a post-processing *ad-hoc* C++ code was used to combine the stored RGB-Depth binary images into an unstructured 3D point-cloud for each measurement time, allowing us to reconstruct the temporal evolution of the flow free surface at the channel-cavity region. Finally, the 3D point-clouds were projected onto a 2D raster grid of $1.4\,mm$ spatial resolution along the x and y coordinates in order to obtain uniformly distributed experimental data of the flow free-surface position at each measurement time. The complete processing procedure is detailed in Appendix C.

2.2. Velocity measurement

Two in-plane components of the velocity were determined at different depths using Particle Image Velocimetry (PIV), according to the experimental setup depicted in Figure 4. A PILS double-cavity Nd:YAG laser (Quanta System) capable of generating 6 ns pulses with a maximum energy of $80\,mJ$ at $532\,nm$ was used as the light source. The point beam was expanded forming a divergent horizontal sheet that covered the whole area of the cavity. Instantaneous image pairs were recorded with a $1024 \times 1344\,pixels$ 12-bit CCD camera (Hamamatsu Photonics) equipped with a $50\,mm$ F#1.2 lens (Nikon Corporation) placed perpendicular to the laser sheet above the channel-cavity region to avoid geometric distortions. The field of view of the CCD camera was $170 \times 223\,mm$ which resulted in a resolution of $166\,\mu m/pixel$. It was determined imaging a grid exactly overlapping the laser sheet. The time interval between the two images in each pair was fixed to $1\,ms$. Recording frequency was 8 frames per second.

For each experiment, the 2D velocity field at the opening of the cavity region at different depths was measured. Initially, the distance between the measurement plane and the flume floor was $a = 1\,cm$ for all the experiments. With increasing water flow rates and hence increasing flow depths, measurements were also obtained for laser plane heights of both $a = 2\,cm$ and $a = 3\,cm$ above the flume floor as the flow depth allowed it. For each one of the measurement planes, 200 image pairs were acquired. Image pairs were processed using the CCD-PIV software code developed at the LTRAC in Monash University [39]. Analysis was performed in $32 \times 32\,pixel$ windows with 50% overlap resulting in maps with 82×62 velocity vectors. To obtain time-averaged velocities at each measurement plane, the 200 instantaneous velocity maps were averaged. Finally, in order to obtain an assembled 2D velocity field for each experiment, the time-averaged velocity maps were averaged along the flow depth.

It must be noted that velocity and surface deformation could not be measured simultaneously, as the water had to be made opaque for the RGB-D sensor. Furthermore, the spatial deformation introduced by the free surface oscillations into the PIV images were determined by a previous analysis of the spatial distortion of a black-white $1 \times 1\,cm$ squares check-board placed at different water depths. The maximum spatial distortion under seiche regime caused by the free surface movement was found at the corner squares of the check-board and was lower than 5% the original square side.

3. Mathematical and numerical modelling

3.1. Governing equations

The flows herein considered are modelled by a 2D depth-averaged hydrostatic model, which accounts for bed topography, friction and turbuent mixing [34]. The choice of this model is motivated by the advantageous ratio between accuracy and computational cost it provides when dealing with multi-scale and large scale flows. Detailed 3D LES models proved to be more accurate as they are able to resolve

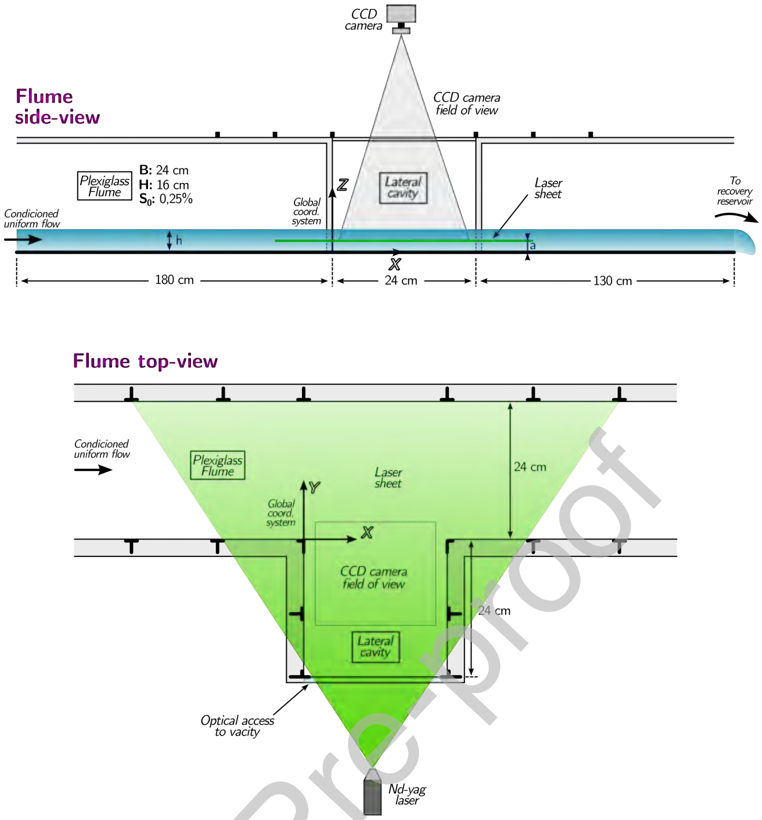

Figure 4: Experimental setup for the velocity measurement using PIV: (top) side-view and (bottom) top-view.

the small features of the flow without extra assumptions, however, they become unaffordable when dealing with multi-scale flows and very large computational domains. By contrary, SWE-based models are able to provide fast predictions of transient events in presence of turbulence and gravity waves in very large domains, at the cost of producing higher discrepancies between the numerical solutions and the physical phenomena of interest. Details about the SWE model used in this study and the numerical scheme are detailed in Appendix A.

3.2. Model configuration

The computational domain used in the simulation is given by $\Omega = [-600, 1200] \times [-240, 240]$ mm and the simulation time is set to $t = 60$ s, which proved to be sufficient for the solution to reach a limit cycle (i.e. a periodic shedding of vortices). The computational mesh is constructed using square cells with $\Delta x = 2.4$ mm, which yields to a solution within the asymptotic range as shown in [34] for a very similar test case. The grid convergence index (factor of safety 1.25) is around 0.5 % for the pair of grids with $\Delta x = 2.4$ and $\Delta x = 1.2$ mm. The CFL number is set to 0.45. The turbulence model parameters, λ and β, are chosen as in [34]. The channel bed roughness coefficient is set to $n_b = 0.01$ sm$^{-1/3}$ The boundary conditions are imposed using the characteristic variables. The unitary discharge is imposed upstream whereas the water depth is imposed at the outlet. Both are constant values in time.

4. Results

In this section, the experimental results for the open channel with lateral cavity configuration detailed in Section 2 are presented. Furthermore, the numerical results obtained with the model presented in Appendix A are also reported for comparison. The main experimental measurements are summarized in Table 2 for the five cases considered in the experimental stage. The water depth at the main channel center upstream the cavity, h_{up}, varied from 20 mm (S1) to 35 mm (S5), whereas the Froude number $Fr = U/\sqrt{gh_{up}}$ was between 0.756 (S1) and 0.83 (S5), being $U = Q_{in}/(Bh_{up})$ the averaged velocity at the main channel. The Reynolds number $Re = Uh_{up}/\nu$ was from about 6676 and 16693 for S1 and S5 respectively, being ν the kinematic viscosity of water. For this Froude number range, the seiche exhibits a large ratio between the longitudinal and the transverse mode amplitude. This seiche is observed in all the experiments, being stronger for the cases with higher discharge. The measured periods T_{exp} for the fundamental mode of the longitudinal seiche are presented in Table 2. An analytical estimation of the longitudinal seiche period (fundamental mode) can be calculated considering a purely 1D seiche as [12, 45]:

$$T_{a,1D} = \frac{2L}{c} \tag{1}$$

or a 2D seiche [45]:

$$T_{a,2D} = \frac{2L}{\sqrt{5}c}. \tag{2}$$

where $L = 0.24$ m and $c = \sqrt{gh_{cav}}$, with h_{cav} being the average water depth in the cavity, taken as $h_{cav} \approx h_{up}$. Note that (2) assumes the fundamental mode of the seiche in both the longitudinal and the transverse oscillation. A good agreement between the experimental, T_{exp}, and the theoretical estimations, $T_{a,1D}$ and $T_{a,2D}$, of the seiche period is observed. Regarding the maximum amplitude of the fundamental mode of the longitudinal seiche, denoted as Δh_{L1}, it is one order of magnitude lower than the water depth h_{up} and it is observed to decrease as the discharge in the main channel is reduced. If calculating a dimensionless seiche amplitude as the ratio $\Delta h_{L1}/h_{up}$, it is observed that this quantity is around 0.13 for cases S2, S3, S4 and S4. Contrarily, for S1 the strength of the longitudinal seiche is much lower with $\Delta h_{L1}/h_{up} = 0.086$ (see Table 2).

Case	h_{up} (mm)	Fr (-)	Re (-)	$T_{a,1D}$ (s)	$T_{a,2D}$ (s)	T_{exp} (s)	Δh_{L1} (mm)	$\Delta h_{L1}/h_{up}$ (-)
S1	20	0.756	6675	1.08	0.97	1.00	1.72	0.086
S2	24	0.78	9045	0.99	0.89	0.91	3.19	0.132
S3	28	0.80	11695	0.92	0.82	0.84	3.53	0.126
S4	31	0.813	13857	0.87	0.78	0.80	4.04	0.130
S5	35	0.83	16963	0.82	0.73	0.77	4.29	0.123

Table 2: Experimental parameter of the longitudinal seiche oscillation for each case. Analytical estimations of the longitudinal seiche period are also included.

A sketch of the relevant points and sections, namely P1, P2 and A-A', B-B', C-C' and T-T', used in the analysis of the data is depicted in Figure 5. The location of the measuring sections and points is shown in Table 3.

4.1. Experimental and numerical results comparison

Figure 6 shows a comparison of the measured and computed time-averaged magnitude of the velocity in the PIV measuring area, within the time interval $t = [40, 60]$ s. A representation of the time-averaged velocity components is provided in Figures B.16 and B.17 in Appendix B. Both experimental and numerical results evidence a clear vortical flow circulation inside the cavity. The location of the center of the main vortex is well predicted by the numerical model, however, the magnitude of the

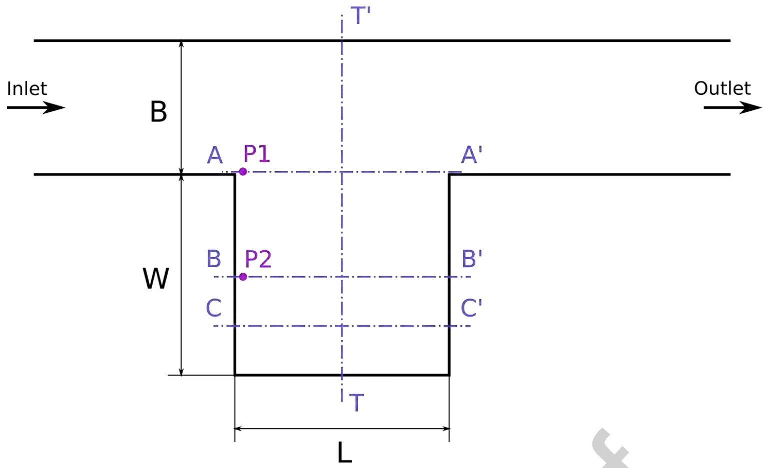

Figure 5: Sketch of the relevant measuring sections and points inside the cavity.

Point/section	x (mm)	y (mm)
P1	2.5	2.5
P2	2.5	-120
A-A'	-	2.5
B-B'	-	-120
C-C'	-	-180
T-T'	120	-

Table 3: Location of the relevant measuring sections and points in Figure 5.

velocity is overestimated near the cavity walls. This behavior has already been reported when using depth-averaged 2D hydrostatic models [12, 34].

Figure 7 shows the spatial distribution of the amplitude of the fundamental seiche frequency, hereafter called longitudinal mode, for the measured and computed water surface elevation, calculated using Algorithm 1 in Appendix D. This representation allows to visually analyze the oscillation patterns in the region of interest (i.e. cavity and channel interaction area). In both the experimental and the numerical results, it is observed that the strongest water surface elevation variations appears inside the cavity and corresponds to the seiche oscillation. Seiche amplitudes range from almost 4.5 mm, for the case S5 to less than 2 mm, for the case S1. The seiche direction is observed to be streamwise, as the oscillation node is located at the section T-T' of the channel-cavity region. This means that the oscillation wavelength is twice the width of the cavity, which agrees with the analytical definition of the seiche in Eq. (1). Both experimental and numerical results show that the strength of the seiche is reduced as moving from the innermost region of the cavity to the positive region of the y axis. Furthermore, a particular oscillation pattern composed of two nodes and three anti-nodes is observed along the shear line at the opening of the cavity (section A-A'), being stronger at the impingement corner ($y = 0$ and $x = 240$ mm). These observations are clearly shown in Figure 8, where a cross-sectional representation in the streamwise direction of the amplitude of the first oscillation mode along A-A' and C-C' is depicted.

In Figure 7, the most noticeable discrepancies between the numerical model and the measured data appear in the main channel area ($y > 0$). A convection effect of the flow in the oscillation is reported in the experimental measurements, showing larger amplitudes downstream the cavity. This effect is not reproduced by the numerical model, which yields a standing oscillation along the middle axis of

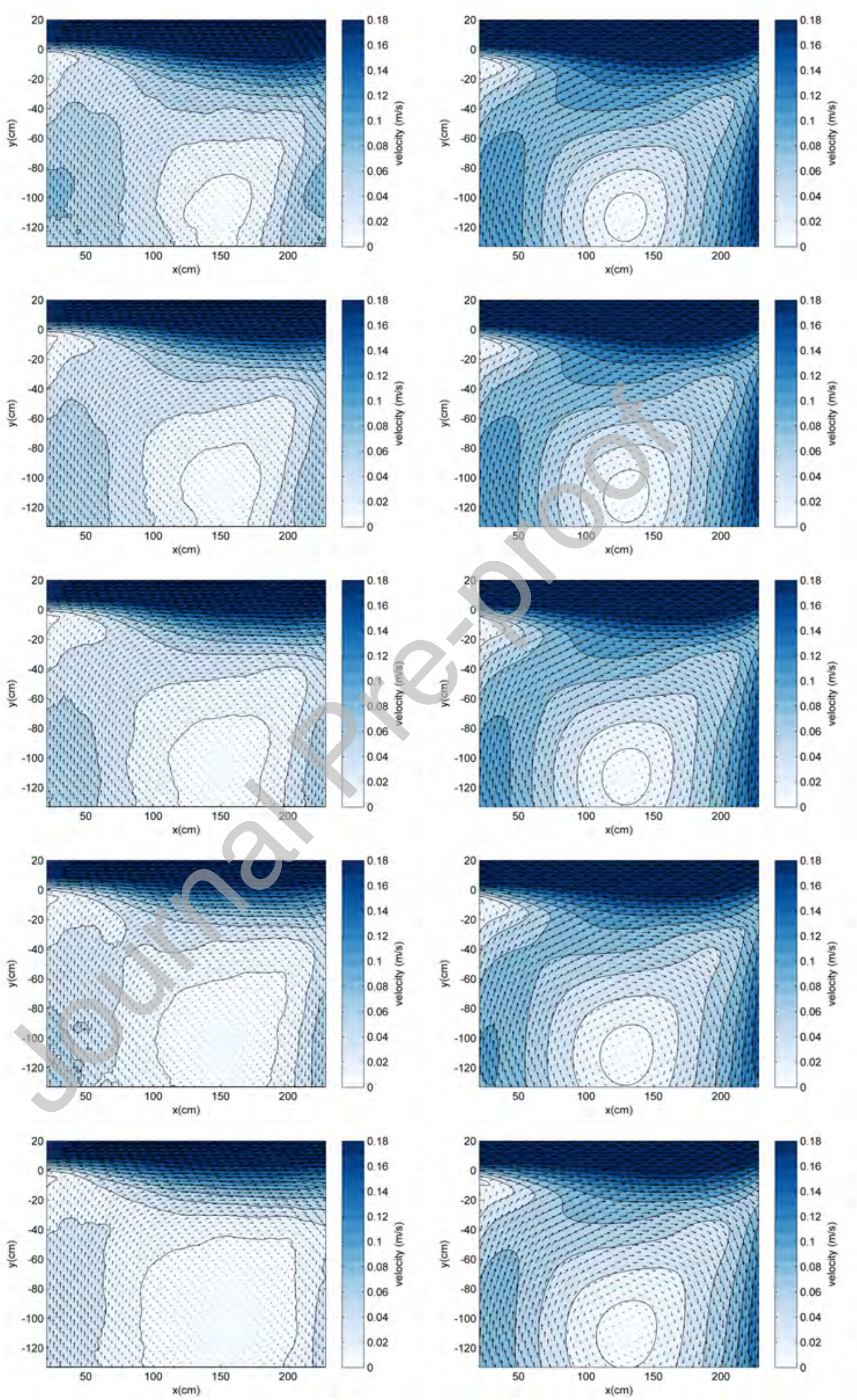

Figure 6: Experimental (left) and numerical (right) time-averaged magnitude of the velocity inside the PIV measuring area. From top to bottom, cases S5, S4, S3, S2 and S1.

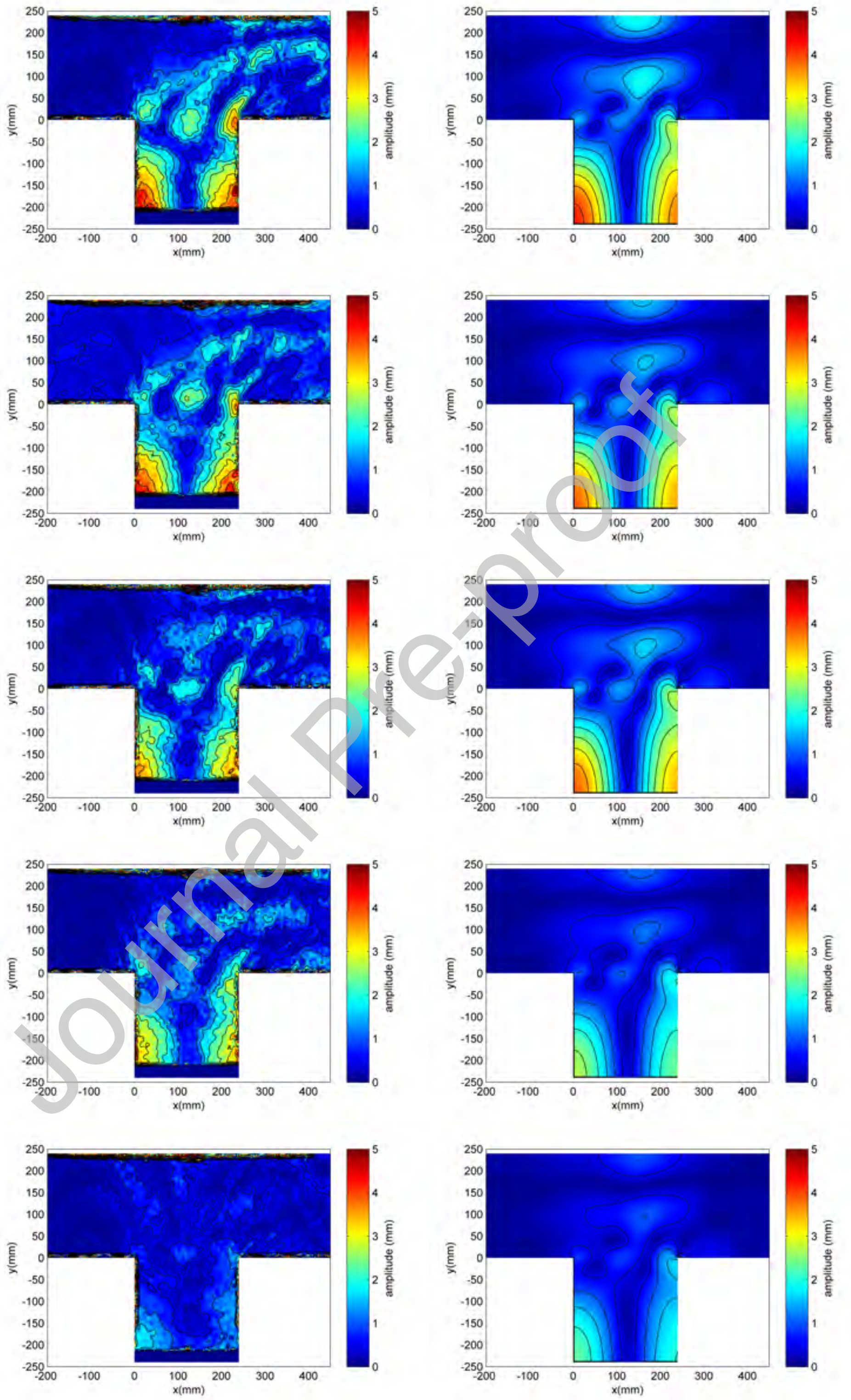

Figure 7: Experimental (left) and numerical (right) amplitude of the oscillation, measured for the longitudinal seiche (fundamental mode). Contour lines are spaced $h = 0.5$ mm.

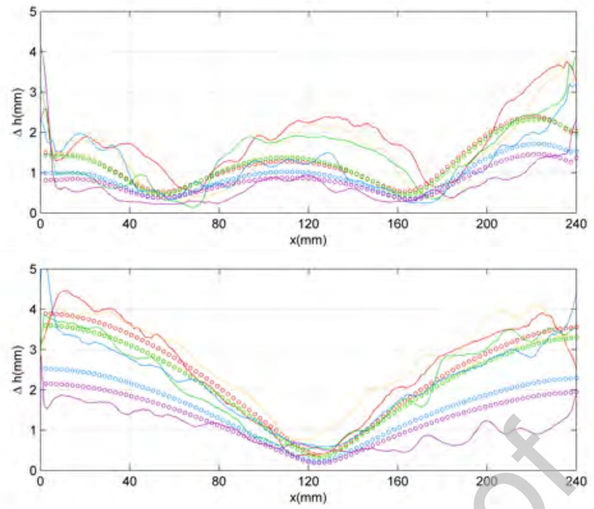

Figure 8: Experimental (solid) and numerical (dots) amplitude of the oscillation along A-A' (top) and C-C' (bottom), for the longitudinal mode, for the cases S1 (purple), S2 (blue), S3 (green), S4 (yellow) and S5 (red).

the cavity, which is not perturbed by the flow in the main channel.

The transverse seiching fundamental mode, of approximately half of the frequency of the longitudinal fundamental mode, has been observed to be very weak in the numerical solutions and absent in the experimental data. A comparison of the experimental and numerical amplitudes of the transverse mode for the cases S5 and S1 is presented in Figure 9. Among all the cases studied, these two cases show the strongest and weakest transverse seiches. The numerical estimation of the magnitude of the maximum amplitude of this seiching mode is 0.5 mm and 0.25 mm, for S5 and S1 respectively, which is one order of magnitude lower than the amplitude of the longitudinal seiche. Such a small magnitude is below the precision of the RGB-D sensor, which has not captured this oscillation mode as shown in Figure 9. This 1/10 relation between the transverse and longitudinal seiche is in good agreement with [11].

For the specific geometrical configuration used in this work, the seiche has been reported to have a bidirectional nature. However, in the cases considered here, it shows a highly dominant longitudinal mode due to the choice of the Froude number. Engelen et al. [11] showed that as the Froude number of the inflow increases, the ratio between the longitudinal and the transverse mode amplitude increases. It is worth noting that, for the case S5, the period of the longitudinal and transverse seiches is 0.72 s and 1.65 s, respectively, whereas for the case S1, these periods are 0.96 s and 1.85 s.

The Fourier spectrum of the water surface elevation and velocity has been computed along sections A-A' and B-B'. The Fourier spectrum for case S5, where the seiche is strongest, is depicted in Figures 10 and 11 for the experimental and numerical water surface oscillation and velocity fluctuations, respectively. Note that the available frequency range of Figure 11 (left) is shorter than the others as the acquisition frequency of the PIV device is lower. The Fourier spectrum distribution of the experimental free surface elevation data evidences that the most energetic oscillation mode is associated to the fundamental mode of the longitudinal seiche, with a measured frequency that is in good agreement with the theoretical estimation (see Table 2). In the numerical results, it is observed that the seiche frequency is slightly over predicted, but the error never exceeds a 10% relative to the experimental value. It is worth noting that the measured and computed velocity oscillation also occurs at the seiche frequency, according to Figure 11. In general, secondary oscillation modes (e.g. second harmonic at $2.6 \sim 2.8$ Hz) are observed to be very weak in the free surface experimental and numerical data. These high-frequency secondary modes are also observed in the computed velocity field but are not detected

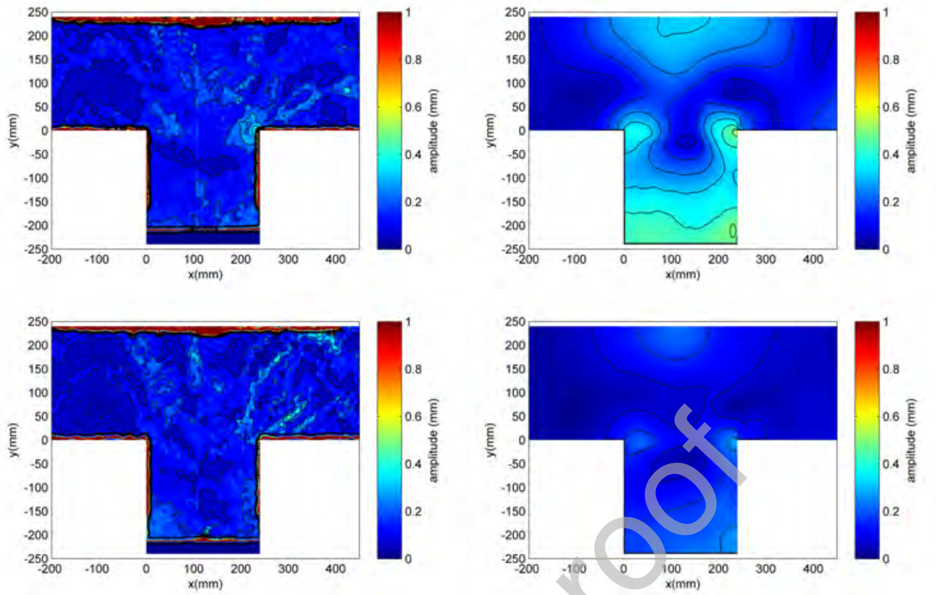

Figure 9: Cases S5 (top) and S1 (bottom). Experimental (left) and numerical (right) amplitude of the oscillation, measured for the transverse seiche.

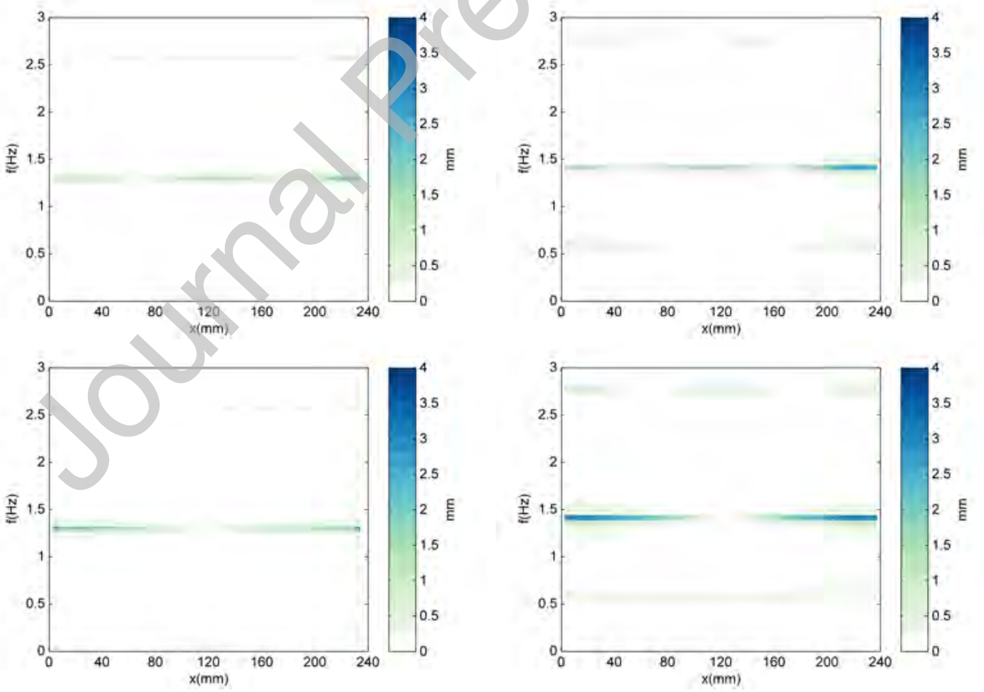

Figure 10: Case S5. Fourier spectrum of the measured (left) and computed (right) water surface elevation along the streamwise direction inside the cavity along the sections A-A' (top) and B-B' (bottom).

in the velocity measurements as they are out of the frequency range of the PIV data. Furthermore, the numerical data shows the presence of a very weak transverse seiche, as discussed before, but the RGB-D sensor and the PIV device have not captured any transverse oscillation.

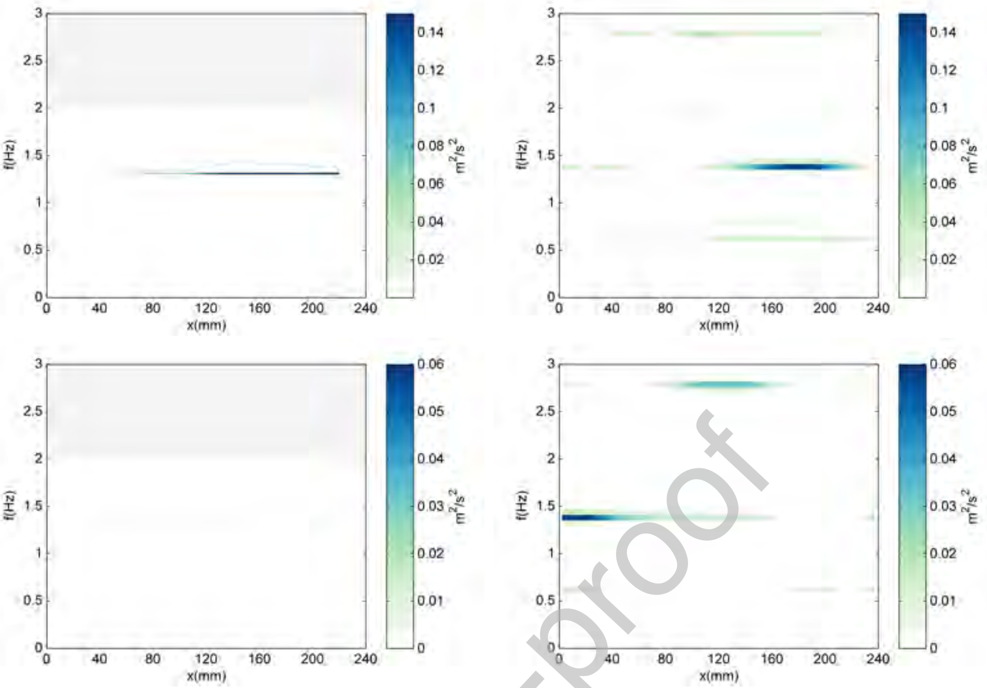

Figure 11: Case S5. Fourier spectrum of the measured (left) and computed (right) velocity magnitude along the streamwise direction inside the cavity along the sections A-A' (top) and B-B' (bottom). The gray shadowed area is beyond the Nyquist frequency.

4.2. Assessment of the mass exchange

The performance of the model to predict the mass exchange between the main channel and the cavity is next assessed. The depth averaged exchange velocity, $E(t)$, and the mass exchange coefficient, k_{veloc}, are used for this evaluation [18, 46]. The former is computed using the distribution of transverse velocity along the mouth of the cavity as follows:

$$E(t) = \frac{1}{L}\int_0^L |v(x,t)|\, dx, \tag{3}$$

with $L = 0.24$ m. A time-averaged exchange velocity along the mouth of the cavity can also be defined as follows:

$$\bar{E}(x) = \frac{1}{T}\int_0^T |v(x,t)|\, dt, \tag{4}$$

with T the integration time. The space-time averaged exchange velocity and mass exchange coefficient are defined as

$$\bar{\bar{E}} = \frac{1}{LT}\int_0^T\int_0^L |v(x,t)|\, dxdt, \qquad k_{veloc} = \frac{\bar{\bar{E}}}{2U}, \tag{5}$$

with U the free stream mean flow velocity in the channel. Note that such coefficients are depth averaged quantities.

Figure 12 shows a comparison between the experimental and numerical time-averaged exchange velocity and streamwise velocity along the mouth of the cavity for test case S3. The model is able to provide a good overall approximation of $\bar{E}(x)$, slightly overestimated for $x/L < 0.3$. The model is also able to provide a good estimation of $\bar{u}(x)$, however, the numerical predictions exhibit a smoother transition at the impingement corner.

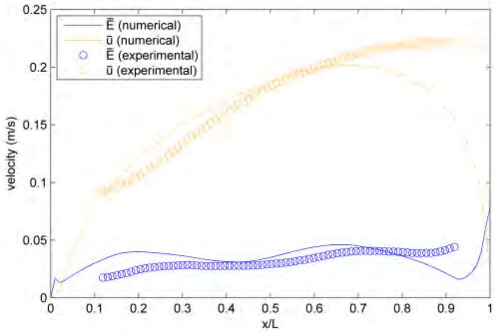

Figure 12: Case S3. Time averaged exchange velocity, $\bar{E}$, and streamwise velocity, $\bar{u}$, along the mouth of the cavity.

The spatial average of $\bar{E}(x)$ in Figure 12 (corresponding to Equation (5)) yields $\bar{\bar{E}} = 0.0321$ m/s and $\bar{\bar{E}} = 0.0349$ m/s for the experimental and numerical data, respectively, showing a good agreement between them. From this, the mass exchange coefficient is computed, yielding $k_{veloc} = 0.038$ and $k_{veloc} = 0.042$ for the experimental and numerical data, respectively. These depth averaged values are in good agreement with $k_{veloc} = 0.02 \sim 0.04$ as reported in [18]. It must be noted that to further investigate the physical mechanisms determining the mass exchange, a complete understanding of the large- and small-scale turbulent structures at the shear layer would be required [33].

4.3. Analysis of the coupling mechanism using the numerical model

The numerical model is used to analyze the coupling mechanism between the vortex shedding at the opening of the cavity, the seiche and the mass exchange between the cavity and the main channel. The transport of a passive solute with a depth-averaged concentration ϕ has been included in the numerical computation of case S3. The solute is injected upstream at $t = 40$ s with a concentration of $\phi = 1$. The diffusion coefficients in Eq. (A.14) are set to zero, i.e. $\epsilon_x = \epsilon_y = 0$. Note that those coefficients account for the mixing processes in the unresolved scales. Setting $\epsilon_x = \epsilon_y = 0$ allows to better understand the relation of the exchange of solute between the main channel and the cavity with the large-scale vortices resolved by the model. It must be borne in mind that in reality, ϵ_x and ϵ_y would be greater than zero as the numerical model does not resolve the small-scale turbulence, where the mixing processes are also relevant.

For the analysis, we define the mass of solute inside the cavity as $m = \int_{\Omega_c} h\phi dA$, with Ω_c the cavity bottom surface, and the flux of solute through the mouth of the cavity $f = dm/dt$. Figure 13 shows the computed water depth at the upstream (P2) and downstream edges, the mass of solute inside the cavity, the solute flux at the mouth of the cavity, the exchange velocity at the mouth of the cavity and the location of the center of the vortices. The vertical red lines mark the minimum and maximum values of E in a period, at $t = 52.29$ s and $t = 52.56$ s, respectively. At those times, the vorticity (computed and measured) and the solute concentration (computed) have been depicted in Figure 14. A representation of the phase portrait of the computed water depth at P2 (seiche) depth versus vorticity at P1, for $40 < t < 60$, is also shown in Figure 15.

It is observed that the vortices are shed at P1 when the water surface elevation reaches the minimum value of the seiche oscillation at the upstream edge of the cavity and near the maximum at the downstream edge. A green dashed line in Figure 13 shows the time at which the vortex is emitted ($t = 52.78$ s). This is also observed in the phase portrait of Figure 15, where the emission point corresponds to the point of maximum vorticity (at P1) and minimum water depth (at P2). After its emission, the vortex travels downstream during a time of approximately $1.5T$, with T the seiche period, until it breaks at the impingement corner. At that moment, the water surface elevation is maximum at the upstream edge of the cavity and minimum at the downstream edge. These findings

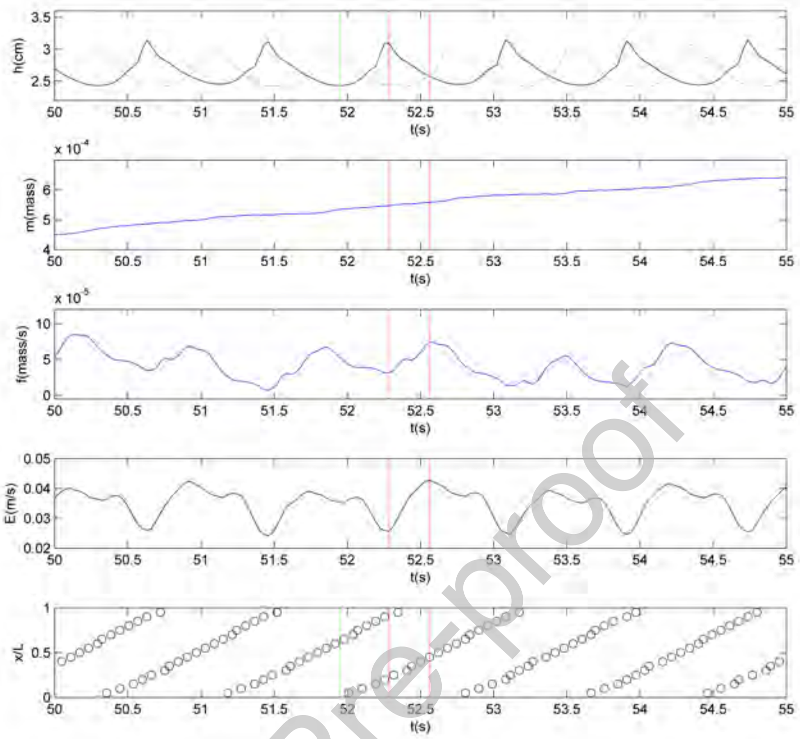

Figure 13: Case S3. Computed water depth at the upstream (black solid line) and downstream edge (gray dashed line), mass of solute inside the cavity, m, solute flux at the mouth of the cavity, f, exchange velocity at the mouth of the cavity, E, and location of the center of the vortices. The vertical red lines mark the maximum and minimum values of E in a period, at $t = 52.29$ and $t = 52.56$ s, respectively. The green line marks the vortex shedding.

are in good agreement with [28]. When the vortex hits the impingement corner, it is split. One part of it is recirculated inside the cavity while the other part is advected downstream in the main channel.

The period of the vortex succession is equal to the seiche period, $T = 1.19$ s. On the other hand, its average wavelength can be approximated from Figure 14 (bottom), yielding $\lambda \approx 2L/3 = 0.16$ m. The relation $v_p = \lambda/T = 0.18$ m/s gives an estimation of an average phase velocity, which is of the order of magnitude of $\bar{u}(x)$ along the mouth of the cavity (see Figure 12). Note that the streamwise velocity of the flow, u, is responsible for the vortex advection along the mouth of the cavity. Since $1 < L/\lambda < 2$, there is a time interval in the seiche period with two vortices coexisting simultaneously in the mixing layer. Note that these findings agree with those in [28], where the relation $\lambda = 2L/3$ was also obtained.

During the seiche period, the minimum and maximum exchange velocities occur at $t \approx t_0 + 0.4T$ and $t \approx t_0 + 0.75T$, with t_0 the vortex emission time. In Figure 13, the vortex emission time is marked in green at $t_0 = 51.95$ s and the minimum and maximum exchange velocities are marked in red, at $t = 52.29$ and $t = 52.56$ s. The vorticity and the solute concentration at those times inside the cavity is depicted in Figure 14. It is observed that the minimum and maximum exchange occur when the vortex is located at $x/L \approx 0.22$ (and second vortex at $x/L \approx 0.95$) and $x/L \approx 0.45$, respectively. It is observed that the time evolution of the mass flow inside the cavity exhibits the same trend as that of the exchange velocity. The maximum and minimum mass flow and exchange velocity happen at the same time, respectively.

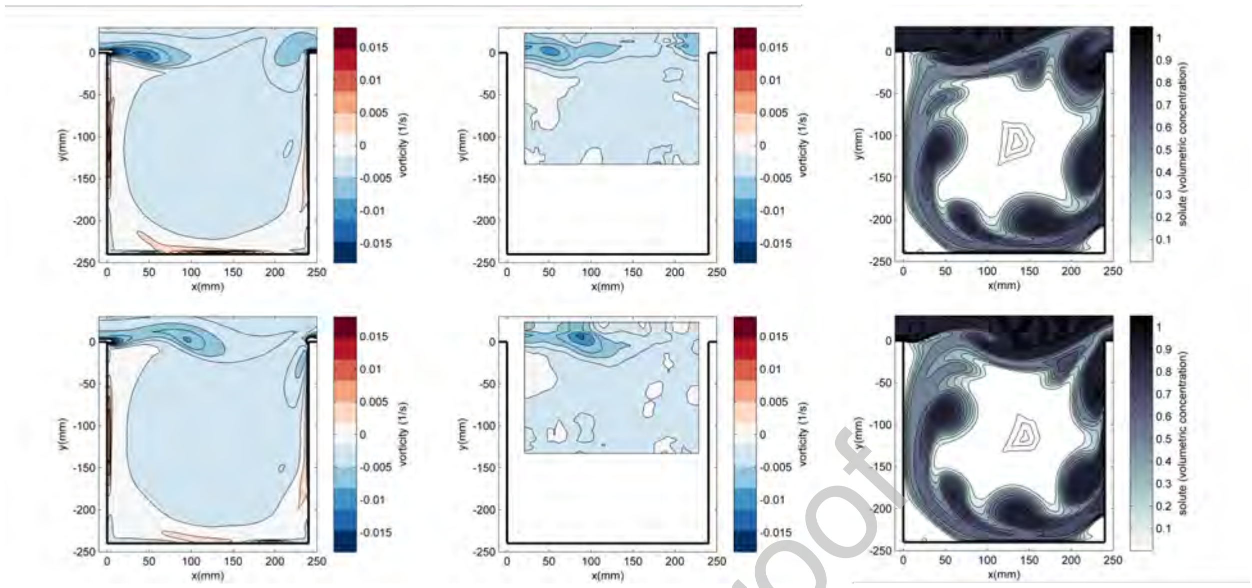

Figure 14: Case S3. Computed vorticity (left), measured vorticity (middle) and computed solute concentration (right) at $t = 52.29$ (top) and $t = 52.56$ s (bottom). The measured vorticity has been improved using an averaging filter.

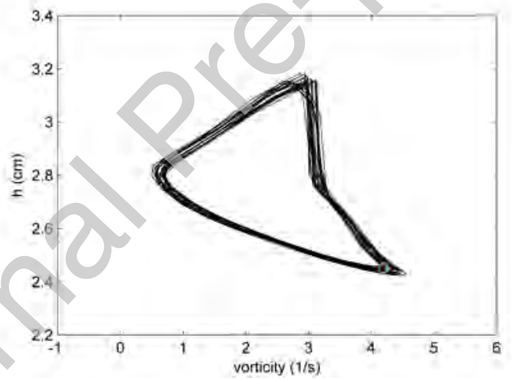

Figure 15: Case S3. Phase portrait of the computed water depth at P2 versus vorticity at P1.

It must be pointed out that the numerical model used in the simulations may increase the sharpness of the seiche, since shock waves in hyperbolic systems are modelled as pure discontinuities. Furthermore, the SWE model works under the assumption of shallowness and hydrostatic pressure, with negligible vertical accelerations. These may be the reasons why the seiche evolution in time shown in Figure 13 (top) exhibits those peaks, differing from a sinusoid.

5. Conclusions

In this work, a high resolution experimental and numerical study of a shallow flow past a channel lateral cavity is presented. Five different experiments are conducted in a large-scale recirculating channel using a fixed Froude number, $Fr = 0.8$. All of them are characterized by the presence of a longitudinal seiche, i.e. a standing gravity wave which is coupled with the hydrodynamical instability at the shear layer. A complete understanding of this resonant phenomenon is of paramount importance to shed light to the mass exchange mechanisms, as the seiche substantially enhances the mixing between the main channel and the lateral cavity.

The main novelty of this work is the use of a pioneering non-intrusive experimental technique to measure the 2D water surface at the channel–cavity area. It must be noted that 2D measurements of transient water surfaces are not usually performed due to the complexity of the traditional measurement techniques. In this work, we use a RGB-D sensing device, which allows to capture a succession of color-coded point clouds at a high frequency. Particle Image Velocimetry measurements are also obtained and are used to carry out a combined study of the water surface evolution and velocity fluctuations at the channel–cavity area, and their interaction. Furthermore, the measured flows are also numerically reproduced using a 2D depth-averaged (DA) URANS high-resolution model which is able to resolve the large-scale coherent vortical structures and model the effect of small-scale turbulence. The high quality of the experimental data reported in this work makes this data set a suitable benchmark for numerical simulation models in order to evaluate their performance in the resolution of turbulent resonant shallow flows.

A frequency analysis of the experimental and numerical data is carried out using the FFT algorithm allowing to obtain 2D high resolution maps of the seiche amplitude for the five different flow configurations. The location of the oscillation nodes and anti-nodes is shown and a good correspondence between experimental and numerical data is reported. The results evidence that the seiche amplitude decreases as the discharge is reduced. On the other hand, the relative seiche amplitude (i.e. seiche amplitude versus water depth ratio) is approximately constant for the experiments S2, S3, S4 and S5. The post-processed spatial distribution of the seiche shows a single oscillation node line along the $T-T'$ section in the inner part of the cavity. Contrary to this, two nodes and three anti-nodes are observed along the opening of the cavity. This particular distribution of nodes and anti-nodes is observed both in the numerical and experimental data. The most relevant difference between numerical and experimental data in the spatial distribution of the seiche is observed at the main channel. The experimental measurements show that the convection effect of the main flow interacts with the seiche, producing larger amplitudes downstream the cavity. Contrarily, the numerical model does not reproduce this effect and shows a more symmetrical distribution of the seiche in the main channel with respect to the middle axis of the cavity.

The Fourier spectrum of the water surface and velocity fluctuations is computed along different cross sections in order to analyze the location of the fundamental oscillation mode and whether or not secondary modes are present. The results evidence that the fundamental mode is associated to the seiche, with a measured frequency close to the analytical estimation. Both the water surface and velocity oscillations match the eigenmode of the cavity and do not show appreciable secondary modes. It must be noted that the numerical model overpredicts the seiche frequency to some extent, but the error never exceeds a 10% relative to the experimental value.

The comparison between the time-averaged PIV velocity data and the numerical predictions also evidences that the experimental and numerical data are in good agreement. It is observed that the numerical model provides a slightly higher velocity magnitude in the recirculation region, as already reported in [34]. This may possibly be due to the fact that the model is 2D and the vertical movement is not allowed, hence the horizontal velocities are overpredicted. In spite of this, the spatial distribution of the time-averaged flow inside the cavity is correctly predicted (e.g. the location of the center of the main vortex). The analysis of the instantaneous vorticity computed from the PIV data shows the periodic shedding of coherent vortices. These observations match the numerical predictions, evidencing that the proposed numerical model is able to resolve the large coherent turbulent fluctuations and to adequately reproduce the transient (resonant) flow.

The model is used to analyze the coupling mechanism between the shedding of vortices (i.e. the selective vortex amplification mechanism), the seiche and the mass exchange between the main channel and the cavity. A comparison of the measured and computed exchange velocity along the shear layer is presented, showing an overall good correspondence between them. A solute transport module is coupled to the hydrodynamic model to simulate the entrainment of solute in the cavity. It is observed that the time evolution of the mass flow inside the cavity exhibits the same trend as that of the exchange velocity.

Acknowledgments

This work was funded by the Spanish Ministry of Science and Innovation under the research project PGC2018-094341-B-I00 (Navas-Montilla, Martnez-Aranda, Garca-Palacn and Garca-Navarro). This work has also been partially funded by Gobierno de Aragn through Fondo Social Europeo: Feder 2014-2020 "Construyendo Europa desde Aragn" (Navas-Montilla, Martnez-Aranda, Garca-Palacn and Garca-Navarro). A. Lozano acknowledges the support of the Regional Government of Aragn to the Fluid Mechanics for a Clean Energy Research Group (T01-17R).

Declaration of interests

The authors report no conflict of interest.

Appendix A. Mathematical and numerical modelling

Appendix A.1. Governing equations

The flows herein considered are modelled by a 2D depth-averaged hydrostatic model. The choice of this model is motivated by the advantageous ratio between accuracy and computational cost it provides when dealing with multi-scale and large scale flows. Detailed 3D LES models proved to be more accurate as they are able to resolve the small features of the flow without extra assumptions, however, they become unaffordable when dealing with multi-scale flows and very large computational domains. By contrary, SWE-based models are able to provide fast predictions of transient events in presence of turbulence and gravity waves in very large domains, at the cost of producing higher discrepancies between the numerical solutions and the physical phenomena of interest. The SWE are expressed in matrix form as follows [34]:

$$\frac{\partial \mathbf{U}}{\partial t} + \frac{\partial \mathbf{F}(\mathbf{U})}{\partial x} + \frac{\partial \mathbf{G}(\mathbf{U})}{\partial y} = \mathbf{S} + \mathbf{D}\,, \tag{A.1}$$

with

$$\mathbf{U} = \begin{pmatrix} h \\ hu \\ hv \end{pmatrix}, \quad \mathbf{F} = \begin{pmatrix} hu \\ hu^2 + \frac{1}{2}gh^2 \\ huv \end{pmatrix}, \quad \mathbf{G} = \begin{pmatrix} hv \\ hvu \\ hv^2 + \frac{1}{2}gh^2 \end{pmatrix}, \tag{A.2}$$

where g is the acceleration of gravity, h is the water depth, hu and hv are the depth averaged unitary discharges in the x and y direction, respectively. The longitudinal and transverse velocities, u and v are depth-averaged mean components in the term of the definition of the Reynolds decomposition. The water depth, h, also corresponds to a mean value.

The source term, $\mathbf{S} = \mathbf{S_z} + \mathbf{S_f}$, accounts for the stress exerted by the bottom topography, $\mathbf{S_z}$, (i.e. bed slope source term) and by the bed roughness, $\mathbf{S_f}$ (i.e. friction source term) and are written as:

$$\mathbf{S_z} = \begin{pmatrix} 0 \\ -gh\frac{dz}{dx} \\ -gh\frac{dz}{dy} \end{pmatrix}, \quad \mathbf{S_f} = \begin{pmatrix} 0 \\ -c_f\,|\mathbf{u}|\,u \\ -c_f\,|\mathbf{u}|\,v \end{pmatrix}, \tag{A.3}$$

where $|\mathbf{u}| = \sqrt{u^2+v^2}$ is the velocity magnitude, $z = z(x, y)$ represents the bottom topography and c_f is the friction coefficient, computed by means of Manning's formulation as follows:

$$c_f = \frac{gn^2}{h^{1/3}}\,. \tag{A.4}$$

where n is the Manning coefficient. Using the Manning roughness coefficient for the estimation of the shear stresses in the flow could not be optimal in some regions inside the cavity. However, this formulation is the most adequate for other regions of the domain and is generally adopted. On the other hand, the term $\mathbf{D}$ includes the molecular and the turbulent stresses in the momentum equations according to the (U)RANS approach and considering the Boussinesq approximation [34], $\mathbf{D} = (0, \tau_x, \tau_y)^T$, where :

$$\mathbf{T} = \begin{pmatrix} \tau_x \\ \tau_y \end{pmatrix} = \nabla\cdot(\nu h \nabla \mathbf{u}) + \nabla\cdot(\nu_t h \mathbf{K}) \tag{A.5}$$

with $\mathbf{K} = \frac{1}{2}(\nabla\mathbf{u} + (\nabla\mathbf{u})^T)$ the strain rate tensor, ν the kinematic viscosity of the fluid and ν_t the turbulent (eddy) viscosity, computed with a suitable closure equation. Note that under the Boussinesq approximation, the Reynolds stress tensor is proportional to the mean strain rate tensor. Different formulations of the viscous and turbulent diffusion terms in (A.5) can be found in the literature

[40, 12, 41, 42]. Here, the approach provided in [41, 42, 43] is considered. The diffusion terms are thus expressed as $\mathbf{D} = \mathbf{D_x} + \mathbf{D_y}$, with:

$$\mathbf{D_x} = \frac{\partial}{\partial x}\begin{pmatrix} 0 \\ hT_{xx} \\ hT_{yx} \end{pmatrix}, \quad \mathbf{D_y} = \frac{\partial}{\partial y}\begin{pmatrix} 0 \\ hT_{xy} \\ hT_{yy} \end{pmatrix}, \tag{A.6}$$

where T_{xx}, T_{xy}, T_{yx} and T_{yy} are the depth-averaged stresses, which read [42]:

$$T_{xx} = 2(\nu + \nu_t)\frac{\partial u}{\partial x}, \tag{A.7}$$

$$T_{xy} = T_{yx} = (\nu + \nu_t)\left(\frac{\partial u}{\partial y} + \frac{\partial v}{\partial x}\right), \tag{A.8}$$

$$T_{yy} = 2(\nu + \nu_t)\frac{\partial v}{\partial y}. \tag{A.9}$$

The depth-averaged mixing length model is used to compute ν_t as:

$$\nu_t = \sqrt{(\nu_t^v)^2 + (\nu_t^h)^2} \tag{A.10}$$

where ν_t^v and ν_t^h are the 3D and 2D eddy viscosities. The 3D component is mainly produced due to the bed friction and it is calculated as:

$$\nu_t^v = \lambda U^* h, \tag{A.11}$$

where λ is an empirical coefficient, $U^* = \sqrt{c_f(u^2 + v^2)}$ is the bed shear velocity and c_f is the friction coefficient defined in Equation (A.4). The parameter λ is normally retained as a calibration parameter [42].

Additionally, the horizontal component of turbulence is mainly produced by horizontal velocity gradients and is computed as:

$$\nu_t^h = \beta l_s^2 \sqrt{2\left(\frac{\partial u}{\partial x}\right)^2 + 2\left(\frac{\partial v}{\partial y}\right)^2 + \left(\frac{\partial u}{\partial y} + \frac{\partial v}{\partial x}\right)^2} \tag{A.12}$$

with $l_s = \kappa \ min(c_m h, y_w)$ [42, 40], where c_m is an empirical coefficient [40], y_w is the distance to the nearest wall and β is a calibration constant. It must be noted that a detailed dispersion-diffusion analysis of the numerical scheme would be required for a fine adjustment of β. An implicit LES approach might be suitable for the horizontal unresolved eddies. In this work, we use a previous calibration from [34].

In order to analyze the mass exchange between the main channel and the cavity, an equation for the transport of solute is included in the model:

$$\frac{\partial (h\phi)}{\partial t} + \frac{\partial (h\phi u)}{\partial x} + \frac{\partial (h\phi v)}{\partial y} = \nabla (\mathbf{K}\nabla\phi), \tag{A.13}$$

where ϕ is the depth averaged concentration of a virtual solute and $\mathbf{K}$ is the diffusion matrix which accounts for the under-resolved mixing:

$$\mathbf{K} = \begin{pmatrix} K_L & 0 \\ 0 & K_T \end{pmatrix} = \begin{pmatrix} \epsilon_x h U^* & 0 \\ 0 & \epsilon_y h U^* \end{pmatrix}, \tag{A.14}$$

with ϵ_x and ϵ_y the diffusion coefficients in the x and y directions.

Appendix A.2. Numerical model

The problem to solve is composed by the SWE in (A.1)–(A.2) and some boundary and initial conditions, constituting the following Initial Boundary Value Problem (IBVP):

$$\begin{cases} \text{PDEs:} \quad \dfrac{\partial \mathbf{U}}{\partial t} + \dfrac{\partial \mathbf{F}(\mathbf{U})}{\partial x} + \dfrac{\partial \mathbf{G}(\mathbf{U})}{\partial y} = \mathbf{S} + \mathbf{D} \\ \text{IC:} \quad \mathbf{U}(\mathbf{x}, 0) = \mathring{\mathbf{U}}(\mathbf{x}) \quad \forall \mathbf{x} \in \Omega \\ \text{BC:} \quad \mathbf{U}(\mathbf{x}, t) = \mathbf{U}_{\partial\Omega}(\mathbf{x}, t) \quad \forall \mathbf{x} \in \partial\Omega \end{cases} \tag{A.15}$$

defined in the domain $\Omega \times [0, T]$, where $\Omega = [a, b] \times [c, d]$ is the spatial domain. The initial condition is given by $\mathring{\mathbf{U}}(\mathbf{x})$ and the boundary condition by $\mathbf{U}_{\partial\Omega}(\mathbf{x}, t)$. The spatial domain is discretized in $N_x \times N_y$ volume cells, denoted by $\Omega_{ij} \subseteq \Omega$ and defined as:

$$\Omega_{ij} = \left[x_{i-\frac{1}{2}}, x_{i+\frac{1}{2}}\right] \times \left[y_{j-\frac{1}{2}}, y_{j+\frac{1}{2}}\right], \qquad i = 1, ..., N_x,\ j = 1, ..., N_y \tag{A.16}$$

Cell sizes will be denoted by ϑ_{ij} and considered constant as $\vartheta_{ij} = \Delta x^2$ (i.e. regular Cartesian grid where $\Delta x = \Delta y$). Inside each cell, the conserved quantities are generally defined as cell averages at time t^n as:

$$\overline{\mathbf{U}}_{ij}^{n} = \frac{1}{\vartheta_{ij}} \int_{\Omega_{ij}} \mathbf{U}(\mathbf{x}, t^n) dA \qquad i = 1, ..., N_x,\ j = 1, ..., N_y\,. \tag{A.17}$$

where $dA = dxdy$. Integration of the system in (A.15) over the discrete domain $\Omega_{ij} \times \Delta t$, where $\Delta t = t^{n+1} - t^n$ yields to the following fully-discrete updating formula [34]:

$$\overline{\mathbf{U}}_{ij}^{n+1} = \overline{\mathbf{U}}_{ij}^{n} - \frac{\Delta t}{\Delta x^2}\left(\mathbf{F}_{i+1/2,j}^{-} - \mathbf{F}_{i-1/2,j}^{+}\right) - \frac{\Delta t}{\Delta x^2}\left(\mathbf{G}_{i,j+1/2}^{-} - \mathbf{G}_{i,j-1/2}^{+}\right) + \frac{\Delta t}{\Delta x^2}\left(\bar{\mathbf{S}}_{ij} + \bar{\mathbf{D}}_{ij}\right), \tag{A.18}$$

where $\mathbf{F}_{i\mp1/2,j}^{\pm}$ and $\mathbf{G}_{i,j\mp1/2}^{\pm}$ are the numerical fluxes at cell interfaces and

$$\bar{\mathbf{S}}_{ij} \approx \frac{1}{\Delta t}\int_0^{\Delta t}\int_{x_{i-1/2}}^{x_{i+1/2}}\int_{y_{j-1/2}}^{y_{j+1/2}} \mathbf{S}\, dydx\, d\tau\,, \quad \bar{\mathbf{D}}_{ij} \approx \frac{1}{\Delta t}\int_0^{\Delta t}\int_{x_{i-1/2}}^{x_{i+1/2}}\int_{y_{j-1/2}}^{y_{j+1/2}} \mathbf{D}\, dydx\, d\tau\,. \tag{A.19}$$

are the approximation of the space-time integral of the source terms and diffusion terms inside the cell. Both approximations are explicit and are detailed in [34]. The time step, Δt, is computed dynamically according to the CFL condition to preserve the stability of the numerical solution.

The numerical fluxes are computed as the space-time integral of the numerical fluxes over the cell edges. To construct a numerical scheme of order $(2k-1)$-th, it is sufficient to approximate such integrals using a $(2k-1)$-th order Gaussian quadrature, thus requiring k quadrature points. For the sake of brevity, details of the calculation of the numerical fluxes at those points are not given here and can be found in [34].

Appendix B. Experimental and numerical averaged velocities

Figures B.16 and B.17 show the X and Y components, respectively, of the averaged experimental velocity at the channel-cavity region for all the experiments carried out. The numerical results have also been depicted for comparison. The center of the main cavity vortex can be clearly identified for all the experiments. In general, the numerical method slightly overestimates the depth averaged velocity of the flow.

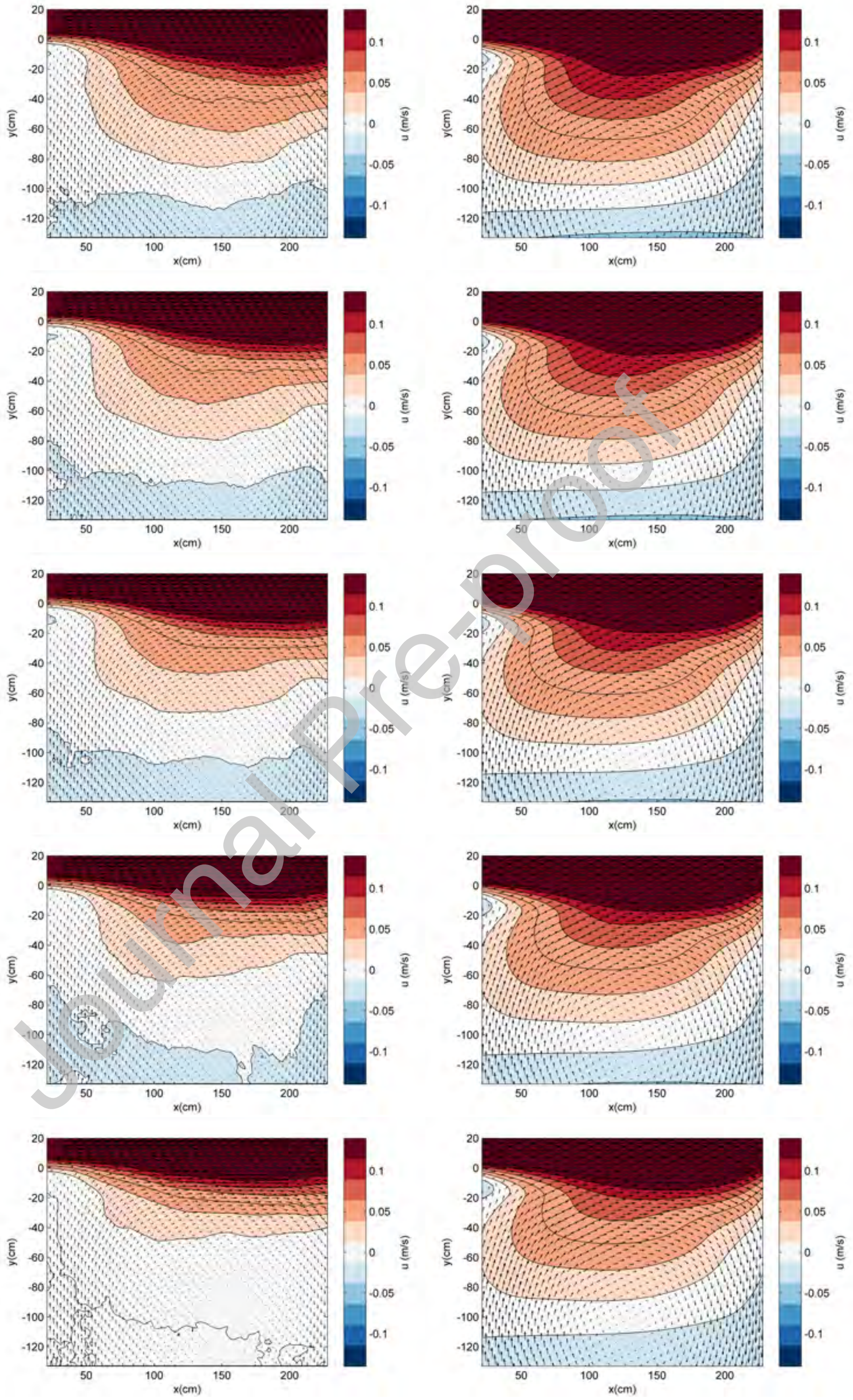

Figure B.16: Experimental (left) and numerical (right) time-averaged streamwise component of the velocity, u, inside the PIV measuring area. From top to bottom, cases S5, S4, S3, S2 and S1.

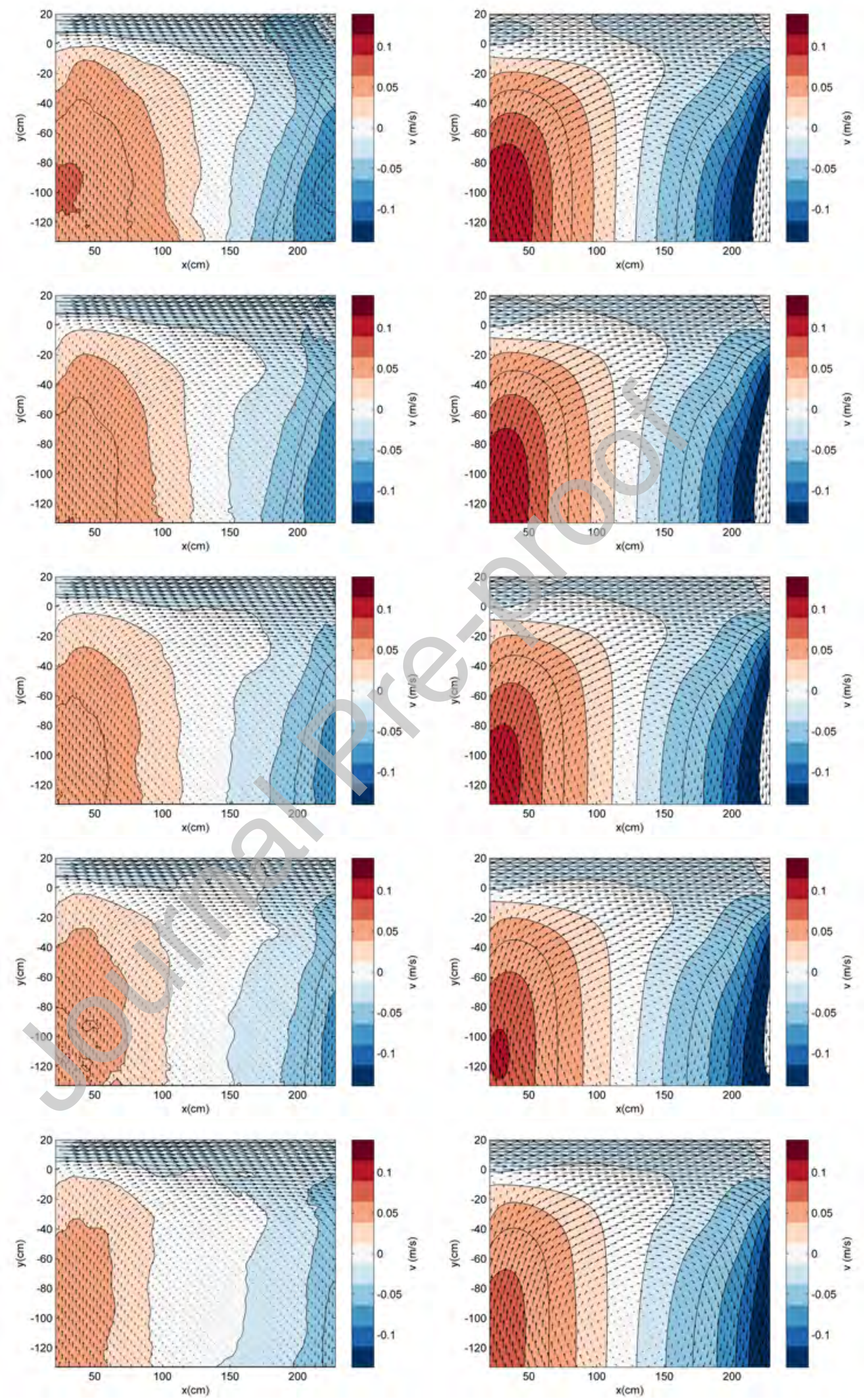

Figure B.17: Experimental (left) and numerical (right) time-averaged spanwise component of the velocity, v, inside the PIV measuring area. From top to bottom, cases S5, S4, S3, S2 and S1.

Appendix C. Kinect data processing

A scheme of the complete procedure to process the raw binary data recorded in laboratory using the RGB-D sensor Microsoft Kinect is shown in Figure C.18. The Kinect device streams a sequence of $640 \times 480\,px$ 8-bit binary RGB images of the objects placed into its field-of-view, together with the corresponding $640 \times 480\,px$ 16-bit binary depth maps. Both the RGB and the depth binary VGA images are directly recorded in a solid-state disk using an *ad-hoc* C++ code based on the open-source *libfreenect* library [38] with an acquisition rate of $30 \pm 2\,Hz$. Each captured RGB and depth binary image is timestamped with millisecond resolution. Then, a post-processing *ad-hoc* C++ code was used to combine the stored RGB-Depth binary images into an unstructured 3D point-cloud for each measurement time. The $X - Y$ spatial resolution of the resultant 3D point-cloud and the depth accuracy (Z axis) depend on the distance between the sensor and the measured surfaces [37]. For the experimental setup used in this work, with a separation of $70\,cm$ approximately between the Kinect sensor and the measured surfaces, the spatial resolution was $1.4 \pm 0.1\,mm$ and the depth accuracy was estimated as $1.5 \pm 0.5mm$ based on previous works [35]. The 3D point-clouds are projected onto a 2D raster grid of the same $X - Y$ spatial resolution as the point-cloud using an *ad-hoc* Matlab code. This allows to obtain uniformly distributed experimental data of the flow free-surface position at each measurement time. The final step of the processing is carried out using *ad-hoc* Python filters in Paraview in order to perform the proper reconstruction of the three-dimensional surfaces.

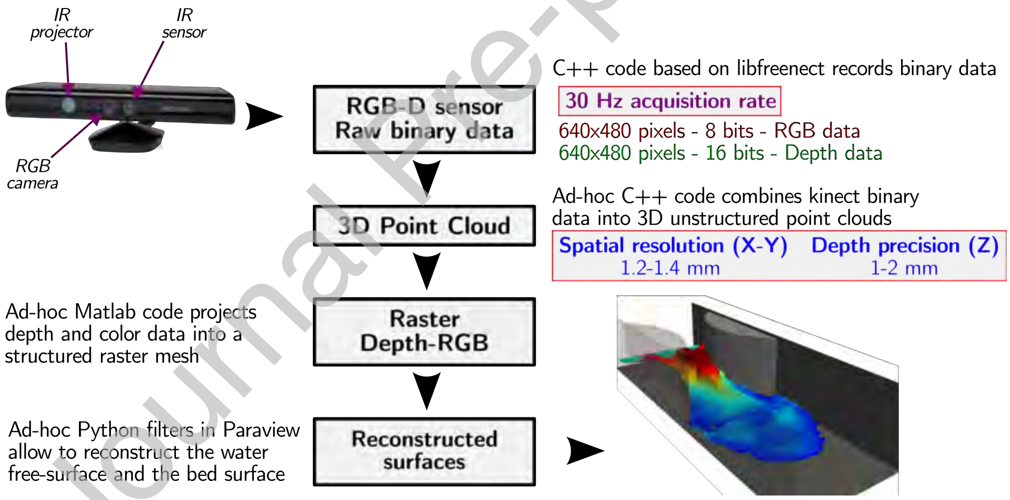

Figure C.18: Scheme of the Kinect raw data processing.

Appendix D. Spectral analysis of the free surface evolution

Seiche amplitude distribution plots can be extracted from the numerical solution using Algorithm 1, where a set of n 2D water surface distribution matrices (i.e. computational grid cells), spaced in time T_s, are the input data and a 2D seiche amplitude distribution matrix is given as output (i.e. $\Delta h[i,j]$). This algorithm is based on the application of the Fast Fourier Transform (FFT) to each grid cell. Note that the sught mode is identified using a search range given by $[f_l, f_r]$, where $f_l = f_1 - \delta$ and $f_r = f_1 + \delta$, f_1 is the theoretical seiche frequency of the sought mode and δ is a tolerance.

Algorithm 1 Spectral analysis of the free surface evolution

procedure SeicheAnalysis2D
initialization:
    $\{px, py\} \leftarrow$ image (raster) resolution
    $n \leftarrow$ number of frames
    $T_s \leftarrow$ sampling time
    $\eta[1:px, 1:py, 1:n] \leftarrow$ recorded frames of surface evolution
matrix loop:
    for $i = 1 : px$ **do**
        for $j = 1 : py$ **do**
            $\eta_{ij} \leftarrow \eta[i, j, :]$ ▷ extracting time evolution at each pixel
            $\hat{\eta}_{ij} \leftarrow \mathrm{FFT}(\eta_{ij})$ ▷ applying the Fast Fourier Transform (FFT)
            $\hat{\eta}_{ij} \leftarrow \left|\frac{\hat{\eta}_{ij}}{n}\right|$ ▷ normalization using the number of samples
            $\hat{\eta}_{ij} \leftarrow \hat{\eta}_{ij}[1 : n/2 + 1]$ ▷ choosing half of the symmetric spectrum
            $\hat{\eta}_{ij} \leftarrow 2 \times \hat{\eta}_{ij}$ ▷ redistributing energy in half-spectrum
            $\hat{\eta}_{ij}[1] \leftarrow 0$ ▷ removing the offset
            $\Delta h[i, j] \leftarrow \max\{\hat{\eta}_{ij}\}_{[f_l, f_r]}$ ▷ most energetic mode within $[f_l, f_r]$

References

[1] G. Jirka and W. Uijttewaal, Shallow Flows: a definition, in GH Jirka and WSJ Uijttewaal (eds), Shallow Flows. CRC Press / Balkema - Taylor and Francis Group, Leiden, International symposium on shallow flows, Delft, 2003.

[2] W. Uijttewaal, Hydrodynamics of shallow flows: application to rivers, Journal of Hydraulic Research, 52 (2014) 157-172.

[3] K. Nadaoka, H. Yagi, Shallow-water turbulence modeling and horizontal large-eddy computation of river flow, Journal of Hydraulic Engineering, 124 (1998) 493–500

[4] C. Hinterberger, J. Fröhlich, W. Rodi, Three-dimensional and depth-averaged large-eddy simulations of some shallow water flows, Journal of Hydraulic Engineering, 133 (2007) 857–872.

[5] Juez, C., Schrer, C., Jenny, H., Schleiss, A. J., Franca, M. J. Floodplain Land Cover and Flow Hydrodynamic Control of Overbank Sedimentation in Compound Channel Flows. Water Resources Research, 55 (2019) 9072–9091.

[6] V. Nikora, I. McEwan, S. McLean, S. Coleman, D. Pokrajac, R. Walters, Double-averaging concept for rough-bed open-channel and overland flows: Theoretical background. Journal of Hydraulic Engineering, 133 (2007) 873-883.

[7] C. Juez, M. A. Hassan, M. J. Franca, The origin of fine sediment determines the observations of suspended sediment fluxes under unsteady flow conditions, Water Resources Research, 54 (2018) 5654–5669.

[8] C. Juez, I. Bhlmann, G. Maechler, A. J. Schleiss, M. J. Franca. Transport of suspended sediments under the influence of bank macroroughness. Earth Surface Processes and Landforms, 43 (2018) 271–284.

[9] E. Langendoen, C. Kranenburg, R. Booij, Flow patterns and exchange of matter in tidal harbours, Journal of Hydraulic Research, 32 (1994) 259–270.

[10] Engelen, L., Crelle, S., Schindfessel, L., De Mulder, T., Spatio-temporal image-based parametric water surface reconstruction: a novel methodology based on refraction. Measurement Science and Technology, 29 (2018) 035302.

[11] Engelen, L., Perrot-Minot, C., Mignot, E., Riviere, N., De Mulder, T. Experimental study of bidirectional seiching in an open-channel, lateral cavity in the time and frequency domain. Physical Review Fluids (2020) (Accepted paper).

[12] I. Kimura, T. Hosoda, Fundamental properties of flows in open channels with dead zone, Journal of Hydraulic Engineering 123 (1997) 98–107.

[13] Tsubaki, R. & Fujita, I. 2006 Surface oscillations in flow past a side cavity using stereoscopic measurement and POD. Journal of Hydroscience and Hydraulic Engineering 24 (2), 4151.

[14] C. Juez, M. Thalmann, A. J. Schleiss, M. J. Franca, Morphological resilience to flow fluctuations of fine sediment deposits in bank lateral cavities, Advances in Water Resources, 115 (2018) 44-59.

[15] Abad J., Rhoads B., Guneralp I., Garca M., Flow structure at different stages in a meander-bend with bendway weirs, Journal of Hydraulic Research 134 (2008) 10521063.

[16] Ten Brinke W, Schulze F, Van Der Veer P., Sand exchange between groyne-field beaches and the navigation channel of the Dutch Rhine: The impact of navigation versus river flow. RiverResearch and Applications 20 (2004) 899928.

[17] Yossef M, de Vriend H., Sediment exchange between a riverand its groyne fields: Mobile-bed experiment. Journal of Hydraulic Engineering 136 (2010) 610625.

[18] Tuna, B. A., Tinar, E., Rockwell, D., Shallow flow past a cavity: globally coupled oscillations as a function of depth, Experiments in fluids, 54 (2013) 1586.

[19] Uijttewaal, W. S. J., Lehmann, D. V., Mazijk, A. V., Exchange processes between a river and its groyne fields: Model experiments, Journal of Hydraulic Engineering, 127 (2001) 928-936.

[20] Le Coz J., Brevis W., Nio Y., Paquier A., Rivire N., Open channel side-cavities: A comparison of field and flume experiments, RiverFlow, 1 (2006) 145152.

[21] Ekmekci A., Rockwell D. Oscillation of shallow flow past a cavity: resonant coupling with a gravity wave, J. Fluids Struct. 23 (2007) 809.

[22] Meile T., Boillat J.L., Schleiss A.J., Water-surface oscillations in channels with axi-symmetric cavities. J. Hydraul. Res. 49 (2011) 7381.

[23] Wolfinger M., Ozen C.A., Rockwell D., Shallow flow past a cavity: coupling with a standing gravity wave, Phys. Fluids 24 (2012) 104-103.

[24] Sanjou M, Nezu I., Hydrodynamic characteristics and related mass transfer properties in open-channel flows with rectangular embayment zone, Environmental Fluid Mechanics 13 (2013) 527555.

[25] Akutina Y., Experimental investigation of flow structures in a shallow embayment using 3D-PTV, PhD thesis, McGill University, Montreal (2015).

[26] Mignot, E., Pozet, M., Riviere, N., Chesne, S., Bidirectional seiching in a rectangular, open channel, lateral cavity. In Congres franais de mcanique. AFM, Association Franaise de Mcanique (2015).

[27] Mignot E, Cai W, Polanco JI, Escauriaza C, Riviere N., Measurement of mass exchange processes and coefficients in a simplified open-channel lateral cavity connected to a main stream. Environmental Fluid Mechanics, 17 (2017) 429448.

[28] Perrot-Minot, C., Engelen, L., Riviere, N., Lopez, D., De Mulder, T., Mignot, E., Seiches in lateral cavities with simplified planform geometry: Oscillation modes and synchronization with the vortex shedding. Physics of Fluids, 32 (2020) 085103.

[29] Kouyi, G. L., Vazquez, J., & Poulet, J. B. (2003). 3D free surface measurement and numerical modelling of flows in storm overflows. Flow measurement and instrumentation, 14(3), 79-87.

[30] Gomit, G., Chatellier, L., Calluaud, D., & David, L. (2013). Free surface measurement by stereo-refraction. Experiments in fluids, 54(6), 1540.

[31] Cobelli, P. J., Maurel, A., Pagneux, V. & Petitjeans, P. 2009 Global measurement of water waves by fourier transform profilometry. Experiments in Fluid 46,10371047.

[32] A. McCoy, G. Constantinescu and L.J. Weber, Numerical Investigation of Flow Hydrodynamics in a Channel with a Series of Groynes, Journal of Hydraulic Engineering, 134 (2008) 157-172.

[33] P. Ouro, C. Juez, M. Franca, Drivers for mass and momentum exchange between the main channel and river bank lateral cavities. Advances in Water Resources, 137 (2020) 103511.

[34] Navas-Montilla A., Juez, C., Franca, M.J. and Murillo, J., Depth-averaged unsteady RANS simulation of resonant shallow flows in lateral cavities using augmented WENO-ADER schemes, Journal of Computational Physics, 24 (2019) 203–217.

[35] S. Martínez-Aranda, J. Fernández-Pato, D. Caviedes-Voulliéme, I. García-Palacín, and P. García-Navarro, Towards transient experimental water surfaces: a new benchmark dataset for 2D shallow water solvers, Advances in water resources, 121 (2018) 130–149.

[36] D. Caviedes-Voulliéme, C. Juez, J. Murillo, P. García-Navarro, 2D dry granular free-surface flow over complex topography with obstacles. Part I: experimental study using a consumer-grade RGB-D sensor, Computers & Geosciences 73 (2014) 177–197.

[37] K. Khoshelham, S.O. Elberink, Accuracy and resolution of kinect depth data for indoor mapping applications, Sensors, 12 (2012) 1437–1454.

[38] OpenKinect open-source project, `https://openkinect.org`

[39] J. Soria, An investigation of the near wake of a circular cylinder using a video-based digital cross-correlation particle image velocimetry technique, Experimental Thermal and Fluids Science, 12 (1996) 221–233.

[40] L. Cea, J. Puertas, M. E. Vázquez-Cendón, Depth averaged modelling of turbulent shallow water flow with wet-dry fronts, Archives of Computational Methods in Engineering, 14 (2007) 303–341.

[41] B. Yulistiyanto, Y. Zech, W. H. Graf, Flow around a cylinder: Shallow-water modeling with diffusion-dispersion, Journal of Hydraulic Engineering, 124 (1998) 419-429.

[42] W. Wu, P. Wang, N. Chiba, Comparison of five depth-averaged 2-D turbulence models for river flows, Archives of Hydro-Engineering and Environmental Mechanics, 51 (2004) 183-200.

[43] V. Caleffi, A. Valiani, A 2D local discontinuous Galerkin method for contaminant transport in channel bends, Computers & Fluids, 88 (2013) 629-642.

[44] A. Navas-Montilla, J. Murillo, Asymptotically and exactly energy balanced augmented flux-ADER schemes with application to hyperbolic conservation laws with geometric source terms, Journal of Computational Physics 317 (2016) 108–147.

[45] A. B. Rabinovich, Seiches and Harbor Oscillations. Handbook of Coastal and Ocean Engineering, (2018) 243-286.

[46] J. Sandoval, E. Mignot, L. Mao, P. Pastn, D. Bolster, C. Escauriaza, Field and numerical investigation of transport mechanisms in a surface storage zone. Journal of Geophysical Research: Earth Surface, 124 (2019) 938-959.

Declaration of interests

The authors declare that they have no known competing financial interests or personal relationships that could have appeared to influence the work reported in this paper.

Author contribution statement:

- Adrian Navas Montilla: Conceptualization, Methodology, Investigation, Formal analysis, Validation, Software, Writing

- Sergio Martinez: Conceptualization, Methodology, Investigation, Formal analysis, Validation, Software, Writing

- Antonio Lozano: Methodology, Experimental setup, Formal analysis

- Ignacio García Palacín: Methodology, Experimental setup.

- Pilar García Navarro: Conceptualization, Project administration, Funding acquisition, Writing – Review and editing